
DISQ-HNET: A DISENTANGLED QUANTIZED HALF-UNET FOR INTERPRETABLE MULTIMODAL IMAGE SYNTHESIS APPLICATION TO TAU-PET SYNTHESIS FROM T1 AND FLAIR MRI FOR ALZHEIMER'S DISEASE

Agamdeep S. Chopra¹, Caitlin Neher^{1†}, Tianyi Ren^{1†}, Juampablo E. Heras Rivera¹, Mehmet Kurt¹

¹Department of Mechanical Engineering, University of Washington, Seattle, WA

[†]These authors contributed equally
{achopra4, neherc, tr1, jehr, mkurt}@uw.edu

February 27, 2026

ABSTRACT

Tau positron emission tomography (tau-PET) provides an in vivo marker of Alzheimer's disease pathology, but cost and limited availability motivate MRI-based alternatives. This work introduces *DisQ-HNet* (DQH), a framework that synthesizes tau-PET from paired T1-weighted and FLAIR MRI while exposing how each modality contributes to the prediction. The method combines (i) a Partial Information Decomposition (PID) guided, vector-quantized encoder that partitions latent information into redundant, unique, and complementary components, and (ii) a Half-UNet decoder that preserves anatomical detail using pseudo-skip connections conditioned on structural edge cues rather than direct encoder feature reuse. Across multiple baselines (VAE, VQ-VAE, and UNet), DisQ-HNet maintains reconstruction fidelity and better preserves disease relevant signal for downstream AD tasks, including Braak staging, tau localization, and classification. PID based Shapley analysis provides modality specific attribution of synthesized uptake patterns.

Keywords Synthesis, UNet, AutoEncoder, Quantization, PID, PET, MRI, Alzheimer's Disease

1 Introduction

Dementia places an increasing burden on healthcare systems worldwide, with Alzheimer's disease (AD) representing one of the most common cause and a major driver of disability and cost Alzheimer's Association [2024], Livingston et al. [2020]. Biological characterization using biomarkers of amyloid deposition and pathological tau has proven imperative for early detection and tracking Jack et al. [2018]. Within this framework, tau pathology is particularly informative because its topographic progression closely tracks disease stage and clinical decline using Braak staging protocols Braak and Braak [1991, 1995].

Tau positron emission tomography (tau-PET) enables in vivo mapping of neurofibrillary tangle burden and distribution, supporting diagnosis, staging, and prognosis in AD Burnham et al. [2024], Chen et al. [2021], Smith et al. [2019]. Notably, ¹⁸F-flortaucipir is widely adopted and supported by a substantial validation literature Burnham et al. [2024]. However, despite its clinical value, tau-PET

remains difficult to scale in many care settings due to constraints such as scanner and tracer logistics, invasive procedure, high costs, and radiation exposure, which collectively limit accessibility and increase patient burden Leuzy et al. [2025], Lee et al. [2024].

These constraints motivate MRI-based alternatives that aim to recover disease relevant molecular information without requiring PET acquisition. Structural MRI is already integral to dementia workups and provides high-resolution anatomical context with broad availability Frisoni et al. [2010]. Consequently, learning a mapping from one or more routinely acquired modalities to a target modality has become a fast growing direction in medical imaging, such as synthetic CT, synthetic MR, and synthetic PET Dayarathna et al. [2024]. In AD specifically, recent work demonstrates that deep learning based models can map tau-PET patterns from more accessible neuroimaging input signals Lee et al. [2024].

Yet, high fidelity synthesis alone is not sufficient for clinical translation. Current synthesis pipelines often behave as *black boxes*. They can produce visually plausible outputs while obscuring which input modality supports a generated uptake pattern, whether the prediction relies on robust anatomical evidence, and how multimodal interactions contribute to disease relevant signal Yang et al. [2022], Muhammad and Bendeache [2024]. In a multimodal setup, we can infer that information is distributed across (i) *redundant* anatomy present in both modalities, (ii) *unique* contrast specific mechanisms, and (iii) *synergistic/complimentary* signal cues that only emerge when modalities are combined. Standard architectures rarely expose this structure explicitly, leading to signal entanglement and attribution ambiguity, precisely when interpretability matters most for downstream analysis.

Two architectural design patterns, while effective for reconstruction, further complicate attribution. First, UNet-based skip connections provide a high-bandwidth shortcut from encoder to decoder Ronneberger et al. [2015], Isola et al. [2017], allowing low-level structure to bypass the latent bottleneck. When powerful decoder pathways exist, the pressure on the bottleneck to encode task relevant factors is reduced, a phenomenon related to latent under-utilization observed in deep generative models Chen et al. [2017] and consistent with information bottleneck theory Tishby and Zaslavsky [2015]. Second, continuous latent vectors can encode heterogeneous mixtures of structure and signal, making it difficult to associate discrete latent factors with interpretable modes of variation. Discrete latent models such as VQ-VAE address part of this challenge by learning a codebook of quantized representations, supporting more structured latents and mitigating failure modes like posterior collapse van den Oord et al. [2017a].

In this work, we target informative multimodal medical imaging. Synthesis that preserves clinically meaningful signals and exposes how these signal pathways contribute to outputs. We propose **DisQ-HNet**, a disentangled quantized Half-UNet framework for multimodal image synthesis, demonstrated on tau-PET synthesis from paired T1-weighted and FLAIR MRI for AD analysis. Our approach is built around a simple idea that interpretability should be architectural, not an afterthought.

We do this by combining:

1. PID-guided disentangled quantization (DisQ-VAE). We draw from Partial Information Decomposition (PID), which decomposes multivariate information into redundant, unique, and synergistic components Williams and Beer [2010], Kolchinsky [2022], Wibral et al. [2017]. By incorporating PID-inspired objectives into a vector-quantized encoder, we explicitly partition latent content into shared, unique, and nontrivial cross-modal signal representations. This makes modality aware attribution a property of the learned latent representations.

2. "Half-UNet" decoder without bottleneck bypass. To preserve structural detail without reintroducing an unin-

terpretable shortcut, we replace standard skip connections with "pseudo-skip" connections, derived from the disentangled redundant bottleneck signals and conditioned on structural edge cues.

In this paper, although we apply the DisQ-HNet framework for tau-PET synthesis, the underlying design targets a general class of multimodal synthesis problems, especially in multimodal medical image synthesis, where synthesis ambiguity must be minimized to preserve clinical trust.

In summary, in this paper we (i) introduce **DisQ-VAE**, a PID-guided, vector-quantized multimodal encoding strategy that factorizes latent information into redundant, unique, and complementary components to enable modality-aware analysis, (ii) propose a **Half-UNet** decoder that preserves structural detail via pseudo-skip connections conditioned on edge cues, improving interpretability, and (iii) combine these into **DisQ-HNet**, a novel framework for interpretable multimodal synthesis, and evaluate it on tau-PET synthesis from T1-weighted and FLAIR MRI with downstream AD relevant analysis.

2 Methods

2.1 Problem setup

Let (x^{T1}, x^{FLAIR}) denote co-registered T1-weighted and FLAIR MRI volumes in a shared anatomical space, and let y denote the corresponding tau-PET target (raw PET in our primary formulation; SUVR is obtained by a deterministic normalization described in §3). Our goal is multimodal synthesis i.e. to learn a conditional generator G_θ that produces $\hat{y} = G_\theta(x^{T1}, x^{FLAIR})$ while (i) preserving high-frequency anatomy and (ii) exposing which portions of the prediction are supported redundantly by both modalities, uniquely by a single modality, or only through their interaction.

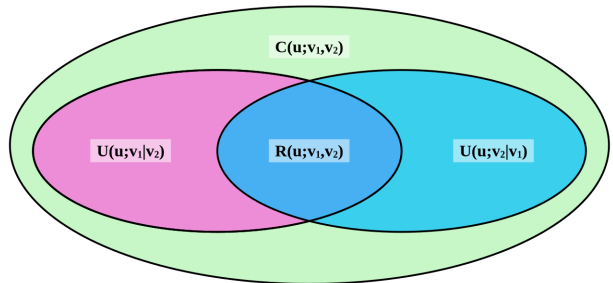


Figure 1: Diagram illustrating the decomposition of mutual information between two inputs (v_1, v_2) and an output u . $R(u; v_1, v_2)$ is the redundant information about u shared by both inputs, $U_{v_1}(u; v_1|v_2)$ and $U_{v_2}(u; v_2|v_1)$ are the unique contributions, and $C(u; v_1, v_2)$ is the complementary (synergistic) contribution. In classical PID these four non-negative terms exactly account for $I(u; v_1, v_2)$.

2.2 Overview of DisQ-HNet

DisQ-HNet couples a *PID-structured, vector-quantized* encoder with an *edge-conditioned Half-UNet* decoder. The model is organized around four components (Fig. 3):

1. **Modality encoders** map each input modality to a continuous latent tensor.
2. **Codebook quantizers** discretize these latents into compact representations van den Oord et al. [2018].
3. **A PID-inspired factorization** allocates discrete latents into *redundant, unique, and complementary* groups (Fig. 1), aligning the representation with interpretable multimodal information components Schick-Poland et al. [2021], Tokui and Sato [2022].
4. **A Half-UNet decoder** reconstructs \hat{y} from the quantized factors, injecting structure through *pseudo-skip connections* derived from gradient map pyramids rather than direct encoder skips connections (Fig. 3).

This design keeps the synthesis pathway *bottleneck-accountable*: structural detail is preserved, but the decoder does not receive a high-bandwidth bypass of the learned factors.

2.3 Quantized latent representation

We build on the VQ-VAE formulation van den Oord et al. [2018]. Given an encoder output $h \in \mathbb{R}^{H \times W \times D \times d}$ and a codebook $\mathcal{E} = \{e_1, \dots, e_K\}$ with $e_k \in \mathbb{R}^d$, quantization maps each latent vector to its nearest code:

$$q(h) = e_{k^*}, \quad k^* = \arg \min_{k \in \{1, \dots, K\}} \|h - e_k\|_2. \quad (1)$$

We use the straight-through estimator to backpropagate through the discrete assignment. The VQ objective comprises (i) a reconstruction term, (ii) a codebook update term, and (iii) a commitment term:

$$\mathcal{L}_{\text{VQ}} = \mathcal{L}_{\text{rec}} + \|\text{sg}[h] - e_{k^*}\|_2^2 + \beta \|h - \text{sg}[e_{k^*}]\|_2^2, \quad (2)$$

where $\text{sg}[\cdot]$ denotes stop-gradient and β controls commitment strength.

2.4 PID-structured disentanglement in discrete space

For two inputs $(x^{\text{T1}}, x^{\text{FLAIR}})$ and target y , PID motivates separating predictive information into *redundant* (R), *unique* ($U_{\text{T1}}, U_{\text{FLAIR}}$), and *complementary* (C) components Williams and Beer [2010], Wibrals et al. [2017]. In our implementation, we enforce this separation directly in the *quantized* latent space using a redundant-unique (RU) encoder applied independently to each modality and a complementary encoder applied to the concatenated modalities, building on vector-quantized representation learning van den Oord et al. [2017b], Razavi et al. [2019]. Let

$$z_1^{\text{RU}} = [r_1, u_1], \quad z_2^{\text{RU}} = [r_2, u_2], \quad z^{\text{C}} = c, \quad (3)$$

where $(r_i, u_i) \in \mathbb{R}^p \times \mathbb{R}^p$ are redundant and unique partitions for modality $i \in \{1, 2\}$, and $c \in \mathbb{R}^p$ is the complementary partition. The RU encoder shares a single codebook \mathcal{E}^{RU} (sliced into \mathcal{E}^{R} and \mathcal{E}^{U}), while c is quantized using a separate complementary codebook \mathcal{E}^{C} .

Differentiable discrete Mutual Information via soft code assignments. Because latents are quantized, we estimate dependence between partitions using a differentiable approximation to discrete mutual information based on soft assignments to codebook entries, analogous to continuous relaxations of discrete variables Jang et al. [2017], Maddison et al. [2017]. For a latent slice z with codebook $\mathcal{E} = \{e_k\}_{k=1}^K$, we define a soft posterior over code indices with temperature τ :

$$\pi(k | z) = \text{softmax}_k \left(-\frac{\|z - e_k\|_2^2}{\tau} \right). \quad (4)$$

For two partitions A and B , we approximate the joint distribution using M sampled latent locations:

$$\hat{p}_{AB}(k, \ell) = \frac{1}{M} \sum_{n=1}^M \pi_A(k | z_A^{(n)}) \pi_B(\ell | z_B^{(n)}), \quad (5)$$

$$\hat{p}_A(k) = \sum_{\ell} \hat{p}_{AB}(k, \ell), \quad \hat{p}_B(\ell) = \sum_k \hat{p}_{AB}(k, \ell). \quad (6)$$

Mutual information (in nats) is then

$$I(A; B) = \sum_k \sum_{\ell} \hat{p}_{AB}(k, \ell) \log \frac{\hat{p}_{AB}(k, \ell) + \epsilon}{(\hat{p}_A(k) + \epsilon)(\hat{p}_B(\ell) + \epsilon)}, \quad (7)$$

which follows the standard discrete mutual information definition Cover and Thomas [2006]. We normalize mutual information by the finite-alphabet upper bound to obtain a bounded dependence measure:

$$\text{NMI}(A; B) = \frac{I(A; B)}{\log(\min(K_A, K_B) + \epsilon)}, \quad (8)$$

consistent with normalized mutual information formulations commonly used in medical imaging Studholme et al. [1999].

PID-inspired mutual information loss. We impose mutual information constraints aligned with the intended role of each partition Williams and Beer [2010], Wibrals et al. [2017]:

- **Redundancy agreement:** the redundant partitions should match across modalities. We therefore encourage high dependence between r_1 and r_2 and explicitly penalize their mismatch in value space.
- **Unique separation:** unique partitions should be modality-specific and non-overlapping; we therefore discourage dependence between u_1 and u_2 .

- **Cross-factor independence:** unique content should not leak into redundant content, and complementary content should remain distinct from both redundant and unique partitions; we therefore discourage dependence between (u_i, r_1) , (c, r_i) , and (c, u_i) .

Concretely, the resulting information loss is:

$$\mathcal{L}_{\text{info}} = \alpha \text{NMI}(u_1; u_2) \quad (9a)$$

$$+ \beta \left(1 - \text{NMI}(r_1; r_2) + \|r_1 - r_2\|_2^2 \right) \quad (9b)$$

$$+ \gamma \left(\text{NMI}(u_1; r_1) + \text{NMI}(u_2; r_1) \right) \quad (9c)$$

$$+ \delta \left(\text{NMI}(c; r_1) + \text{NMI}(c; r_2) \right) \quad (9d)$$

$$+ \epsilon \left(\text{NMI}(c; u_1) + \text{NMI}(c; u_2) \right). \quad (9e)$$

Anti collapse variance floor. To prevent degenerate low variance solutions (particularly for u_1 , u_2 , and c), we add a variance floor penalty computed per channel over sampled latent locations:

$$\mathcal{L}_{\text{vf}}(z) = \frac{1}{C} \sum_{j=1}^C \max(0, \sigma_0 - \text{Std}(z_j)), \quad (10)$$

Where σ_0 is a fixed minimum standard deviation threshold that prevents channel-wise latent collapse by penalizing degenerate low-variance representations C is the number of channels, and z .

$$\mathcal{L}_{\text{info}} = \mathcal{L}_{\text{info}} + \lambda_{\text{vf}} [\mathcal{L}_{\text{vf}}(u_1) + \mathcal{L}_{\text{vf}}(u_2) + \mathcal{L}_{\text{vf}}(c)], \quad (11)$$

This term is lightweight but stabilizes training by discouraging collapse of the unique and complementary partitions while leaving redundancy alignment to the mutual information and value-consistency terms above, similar to capacity-control strategies used to prevent latent collapse in variational models Higgins et al. [2017], Burgess et al. [2018].

Redundant training stabilization. In practice, we recommend enforcing *symmetry* between the two RU branches so that neither redundant pathway becomes consistently ignored by the decoder or under utilized by the codebook. Two simple strategies work well, **(i) random modality swapping** and **(ii) redundant mixing**. For swapping, with probability $p = 0.5$ per mini-batch we swap the modality inputs to the RU encoder (i.e., exchange x^{T1} and x^{FLAIR} before computing z_1^{RU} and z_2^{RU}). This removes persistent ordering cues and forces the model to treat the redundant channel as modality agnostic, rather than implicitly bias one stream. For mixing, we sample $\alpha \sim \mathcal{U}(0, 1)$ and form an interpolated redundant representation $r_{\text{mix}} = \alpha r_1 + (1 - \alpha) r_2$, then use r_{mix} in place of r_1 or r_2 (or stochastically choose between $\{r_1, r_2, r_{\text{mix}}\}$) when assembling the decoder input. This encourages both redundant partitions to remain predictive and aligned, complementing the explicit $(1 - \text{NMI}(r_1; r_2)) + \|r_1 - r_2\|_2^2$

term, and empirically reducing failure modes where one branch carries most of the redundant content while the other collapses or drifts. We deploy these operations as training regularizers only; inference forward pass uses the first redundant component without swapping or mixing.

2.5 Edge-conditioned Half-UNet decoding

Standard UNet skip connections preserve high-frequency detail but directly bypass the bottleneck, blending encoder features into the decoder and complicating latent analysis Ronneberger et al. [2015]. DisQ-HNet replaces direct skips with *pseudo-skips* derived from a structural edge pyramid computed from the first MRI modality.

3D edge extraction. We compute a volumetric edge magnitude map $M(\mathbf{x})$ from the single-channel MRI input $I(\mathbf{x})$ using a set of 3D Sobel filters in axis and diagonal orientations Sobel and Feldman [1968]. Filter responses are aggregated using an RMS energy measure:

$$M(\mathbf{x}) = \sqrt{\sum_{f=1}^F [(S_f * I)(\mathbf{x})]^2 + \epsilon}, \quad (12)$$

where $\{S_f\}_{f=1}^F$ denotes the 3D Sobel kernels, $*$ denotes 3D convolution, and ϵ ensures numerical stability.

We then apply global min-max normalization:

$$\hat{M} = \frac{M - \min(M)}{\max(M) - \min(M) + \epsilon}, \quad (13)$$

and construct a multi-scale pyramid $\{\hat{M}_\ell\}_{\ell=1}^L$ aligned with decoder resolutions (Fig. 3), following classical multi-resolution analysis principles Burt and Adelson [1983].

Pseudo-skip injection. We inject the quantized latent factors only once to initialize the decoder at the coarsest scale. Structural guidance is then introduced through the edge pyramid as pseudo-skips at subsequent decoder stages. The first decoder feature is initialized as

$$d_L = \phi_L(\eta(z_R, z_U, z_C)), \quad (14)$$

and for $\ell = L - 1, \dots, 0$ we fuse the upsampled feature map with a learned projection of the edge map at the corresponding scale:

$$d_\ell = \phi_\ell \left(\text{UP}(d_{\ell+1}) \parallel \psi_\ell(\hat{M}_\ell) \right), \quad (15)$$

where \parallel denotes channel-wise concatenation, ϕ_ℓ denotes the learnable decoder transformation at stage ℓ , and ψ_ℓ denotes the corresponding learnable projection module of the pseudo-skip pathway at the same resolution.

Edge-supervised skip consistency loss. To explicitly anchor pseudo-skip pathways to anatomical structure, the decoder produces auxiliary skip reconstructions $\{\tilde{M}_\ell\}_{\ell=1}^L$

at multiple resolutions. These are supervised to match the downsampled edge map:

$$\mathcal{L}_{\text{skip}} = \frac{1}{L} \sum_{\ell=1}^L \left\| \mathcal{D}_{\ell}(\hat{M}) - \tilde{M}_{\ell} \right\|_2^2, \quad (16)$$

where $\mathcal{D}_{\ell}(\cdot)$ denotes trilinear downsampling to the spatial size of \tilde{M}_{ℓ} . This encourages the pseudo-skip signals to remain structurally meaningful without introducing direct encoder feature bypass.

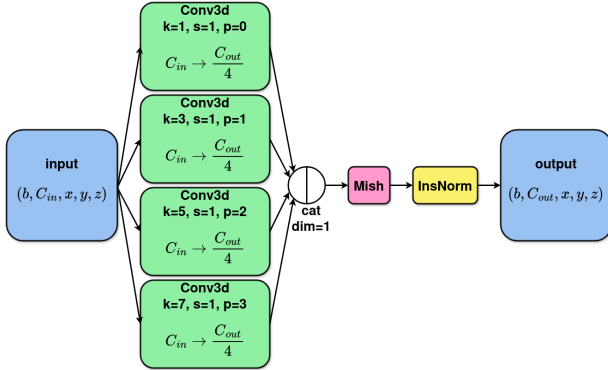


Figure 2: Architecture of inception-based multi-kernel convolution layer (MKConv).

2.6 Training objective and inference

DisQ-HNet is trained end-to-end with a weighted sum of reconstruction, quantization, and information-factorization losses:

$$\mathcal{L} = \mathcal{L}_{\text{rec}}(y, \hat{y}) + \lambda_{\text{vq}} \mathcal{L}_{\text{VQ}} + \lambda_{\text{info}} \mathcal{L}_{\text{info}} + \lambda_{\text{skip}} \mathcal{L}_{\text{skip}}. \quad (17)$$

At inference time, the auxiliary heads for structural reconstruction are dropped during the forward pass, consisting of encoding, quantizing, and decoding to obtain \hat{y} (Fig. 3).

3 Implementation

3.1 Capacity matching

Table 1: Model size in terms of learnable parameters.

Model	Learnable parameters
DQ2H	4,931,877
DQ2H + SPADE	5,153,437
UNet	4,639,196
UNet + SPADE	4,758,532
VAE	5,506,257
VQVAE	4,780,002
DQ2	5,600,856
DQ3	5,307,864

To isolate architectural effects, we implement all models with comparable capacity of approximately 5M parameters as shown in Table 1 Tan and Le [2019], Raghu et al. [2019].

3.2 Common architectural primitives

All models share the same convolutional building block, an Inception-style **multi-kernel 3D convolution module** (Fig. 2) that applies parallel $1 \times 1 \times 1$, $3 \times 3 \times 3$, $5 \times 5 \times 5$, and $7 \times 7 \times 7$ convolutions and concatenates their outputs along the channel dimension Szegedy et al. [2015]. We use Mish activations throughout Misra [2019]. Resolution changes follow a consistent pattern. Encoder stages downsample using stride-2 3D convolutions Ronneberger et al. [2015], while decoder stages upsample using trilinear interpolation followed by multi-kernel refinement Isola et al. [2017]. Lightweight $1 \times 1 \times 1$ residual projections are used between scales to align channel dimensions He et al. [2016].

3.3 Normalization and SPADE conditioning

We use **InstanceNorm3d** in all layers by default Ulyanov et al. [2016]. When SPADE conditioning is enabled, we *replace normalization layers in the decoder only* with SPADE blocks Park et al. [2019]; encoders remain InstanceNorm3d. This keeps the encoder representation comparable across variants while allowing spatially adaptive modulation inside the synthesis pathway.

3.4 DisQ-HNet

Our primary contribution, **DQH**, specifically the DQ2H variant (Fig. 3), comprises two vector-quantized encoders and a structural decoder as such:

Quantized encoders. DQ2H uses (i) an **RU encoder** operating on a single-modality input (1 channel) and (ii) a **C encoder** operating on the concatenated modalities (2 channels). Both encoders implement a four-stage pyramid with the shared multi-kernel blocks and stride-2 downsampling at each stage. The RU stream uses channel widths $\{8, 16, 32, 64\}$ and quantizes to a codebook of size $K=4096$ with embedding dimension 64. The C stream uses channel widths $\{4, 8, 16, 32\}$ and quantizes to a separate $K=4096$ codebook with embedding dimension 32. These codebooks parameterize the discrete latent factors used by the decoder (as described in §2.4).

Structural decoder. The decoder begins from the fused quantized representation (concatenated across streams) and reconstructs the PET volume through four upsampling stages with mirrored channel widths, terminating in a $1 \times 1 \times 1$ output projection to a single channel. To preserve anatomical detail without direct encoder-to-decoder feature bypass, we inject multi-scale **pseudo-skip** structural signals (Fig. 3), implemented as shallow projections of the structural pyramid and $1 \times 1 \times 1$ fusion layers at the corresponding decoder resolutions. When SPADE is enabled, only the decoder’s normalization layers are swapped as

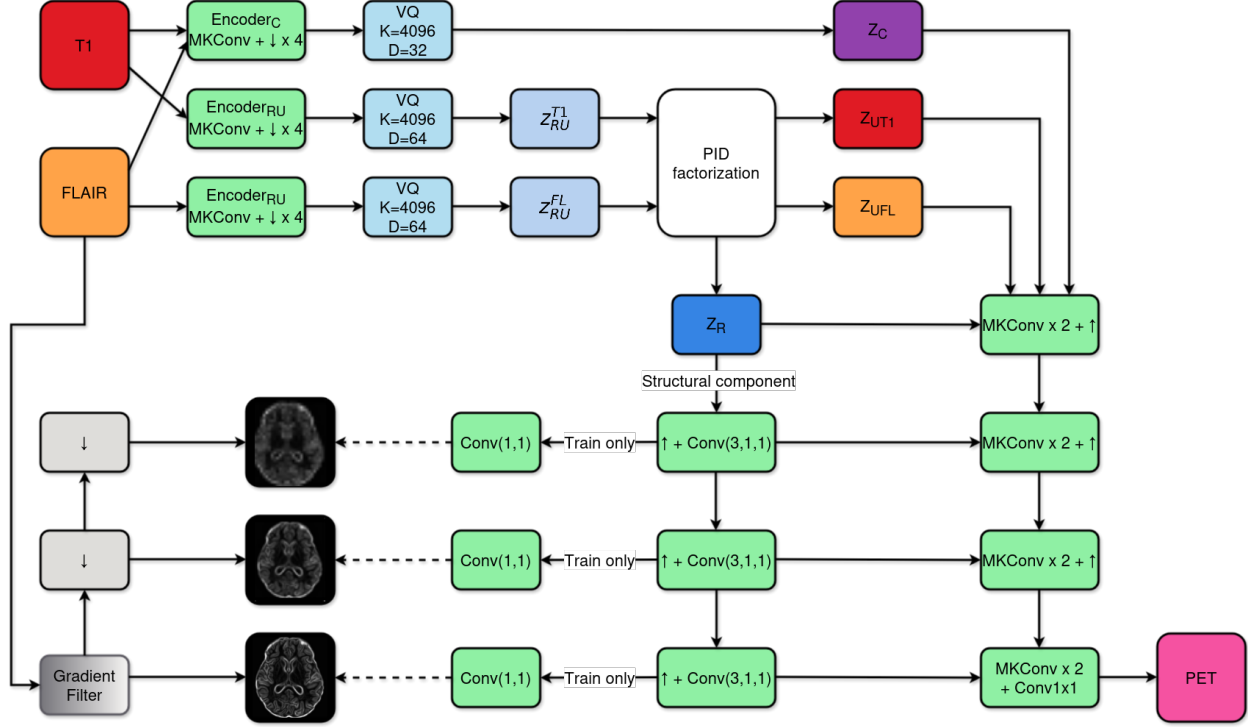


Figure 3: **DisQ-HNet (DQH) with PID-factorized latents and a structural decoder.** T1 and FLAIR are encoded by a shared $Encoder_{RU}$ to produce z_{RU}^{T1} and z_{RU}^{FL} , and by $Encoder_C$ (on concatenated inputs) to produce the complementary latent z_C . Vector quantization (VQ) discretizes these latents. A PID module decomposes the shared representations into redundant z_R and unique components z_{UT1} and z_{UFL} , which are concatenated with z_C to condition the decoder. The decoder synthesizes PET via stacked MKConv blocks with downsampling (\downarrow) in the encoders and upsampling (\uparrow) in the decoder. Pseudo-skip connections upsample structural component of redundant latent using lightweight convolution of kernel size 3, stride 1, and padding 1. These feature maps are conditioned on structural/anatomical features of the input using lightweight train time convolution $1 \times 1 \times 1$ matching outputs of pyramid comprising of sobel-based gradient edge extraction and downsampling

described above; convolutional structure, channel widths, and quantization settings are unchanged.

3.5 Encoder-head variants

We tested two factorization variants, a **three-head** configuration with dedicated encoder heads for the latent factor groups, and a more compact **two-head** configuration (DQ2H) that retains the same quantized factorization while reducing encoder compute. Across our experiments, the **two-head setup provides the best compute and performance trade-off** relative to the three-head alternative. A single unified encoder head is an attractive simplification, but we leave this direction for future exploration.

4 Experiments and Results

We trained all PET synthesis models on combined ADNI-3 Weiner et al. [2017] and OASIS-3 LaMontagne et al. [2019] data, yielding 605 training samples after preprocessing and quality control. Preprocessing included rigid

and affine registration of FLAIR and PET to T1 space, skull stripping, denoising, cropping and resizing, and global intensity normalization. BRAAK staging was derived from SUVR maps by normalizing PET to mean cerebellar gray uptake. Regional mean SUVR was computed in stage defining ROIs: Braak I/II (entorhinal, parahippocampal, hippocampus), Braak III/IV (limbic and temporal cortex), and Braak V/VI (parietal, frontal, and occipital cortices). Subjects were assigned Braak V/VI if $suvr_{ROI_{V/VI}} > 1.3$, else Braak III/IV if $suvr_{ROI_{III/IV}} > 1.2$, else Braak I/II if $suvr_{ROI_{I/II}} > 1.1$, otherwise CN.

Training used random affine augmentation, left right flips, and random resized cropping. The effective batch size was 8 using gradient accumulation, and 64 training cases were sampled per epoch. Models used comparable encoder decoder backbones and parameter counts. Training ran for 1000 epochs with cosine annealing learning rate decay from 10^{-4} to 10^{-5} using AdamW optimizer with default parameters. Vector quantized models used 20 warmup epochs with quantization disabled, followed by k means codebook initialization. We train the vector quantized

Table 2: Validation reconstruction metrics on raw PET and SUVR PET (mean±std over subjects). Best values per column were bolded. RelErr(%) was computed from regional SUVR means as mean absolute percent error aggregated over ROIs and subjects.

Model	Raw PET					SUVR PET					
	MAE ↓	MSE ↓	PSNR ↑	SSIM ↑	MS-SSIM ↑	MAE ↓	MSE ↓	PSNR ↑	SSIM ↑	MS-SSIM ↑	RelErr(%) ↓
VAE-MSE	0.1243	0.0212	16.65	0.838	0.747	0.3684	0.0846	18.30	0.841	0.747	46.3
VQVAE-MSE	0.1215	0.0210	16.91	0.841	0.747	0.3571	0.0784	18.41	0.844	0.751	45.3
UNet-MSE	0.1201	0.0209	17.07	0.854	0.812	0.3528	0.0819	19.08	0.855	0.812	31.2
UNet+SPADE-MSE	0.1072	0.0178	18.31	0.861	0.850	0.2914	0.0543	20.51	0.866	0.857	12.8
UNet+SPADE-AG	0.4219	0.2472	7.52	0.688	0.002	0.9712	0.7751	10.05	0.729	0.020	73.0
UNet+SPADE-VCC	0.1066	0.0175	18.36	0.863	0.854	0.2924	0.0555	20.44	0.868	0.861	13.4
UNet+SPADE-MSE-AG	0.1072	0.0178	18.29	0.863	0.851	0.2938	0.0560	20.43	0.868	0.857	13.7
UNet+SPADE-VCC-AG	0.1063	0.0175	18.37	0.862	0.850	0.2921	0.0555	20.48	0.867	0.857	13.2
DQ2-MSE	0.1152	0.0198	17.48	0.850	0.801	0.3356	0.0754	19.43	0.853	0.798	45.3
DQ3-MSE	0.1272	0.0219	16.69	0.835	0.754	0.3667	0.0838	18.07	0.839	0.762	56.5
DQ2H-MSE	0.1085	0.0178	18.22	0.861	0.842	0.2958	0.0567	20.57	0.865	0.848	15.7
DQ2H-MSE-R18	0.1135	0.0188	17.65	0.852	0.811	0.3252	0.0715	19.70	0.855	0.810	44.6
DQ2H-MSE-Inf-R18	0.1093	0.0181	18.13	0.858	0.837	0.3033	0.0604	20.37	0.861	0.840	26.6
DQ2H-MSE-Inf	0.1043	0.0168	18.53	0.862	0.848	0.2918	0.0538	20.54	0.866	0.855	13.1
DQ2H-VCC-Inf	0.1088	0.0182	18.06	0.855	0.835	0.3044	0.0625	20.14	0.859	0.839	25.6
DQ2H+SPADE-MSE-Inf	0.1093	0.0181	18.12	0.856	0.831	0.3016	0.0619	20.29	0.860	0.837	16.6
DQ2H+SPADE-VCC-Inf	0.1084	0.0180	18.12	0.857	0.839	0.3074	0.0641	20.14	0.860	0.843	23.1

models with exponential moving average (EMA) codebook updates, where each embedding is updated from running averages of assigned latent vectors and counts to provide stable codebook adaptation and reduce collapse.

We evaluated three baselines, a continuous VAE, a discrete VQ-VAE, and a direct regression UNet, alongside our proposed DQ models. These baselines represented continuous latent bottlenecks, discrete codebook bottlenecks, and deterministic paired translation, providing a compact comparison set without introducing large changes in compute or inductive bias from heavier generative families.

MSE served as the default reconstruction objective to ensure a stable and fair baseline across architectures LeCun et al. [1998]. In particular for *quantized* variants, the smooth quadratic objective encourages consistent early optimization and more uniform code utilization, which empirically reduces premature codebook collapse during and after the warm-up period van den Oord et al. [2017a], Razavi et al. [2019].

We also evaluated two high contrast preserving reconstruction losses used to reduce over-smoothing in image synthesis Ledig et al. [2017]. First, we used an voxel-wise contrast-weighted Charbonnier loss, i.e., a robust ℓ_1 -like penalty reweighted by the target’s local gradient magnitude:

$$\rho(r) = \sqrt{r^2 + \varepsilon^2}, \quad w_i = 1 + \alpha \|\nabla y\|_i^\gamma, \quad (18)$$

$$\mathcal{L}_{VCC} = \frac{1}{N} \sum_{i=1}^N w_i \rho(\hat{y}_i - y_i), \quad (19)$$

where y and \hat{y} denote the target and prediction, ∇y is computed using finite differences, and α, γ control the emphasis placed on high-contrast voxels. This formulation upweights residuals near sharp transitions (large $\|\nabla y\|$) while retaining robustness to outliers via the Charbonnier penalty Charbonnier et al. [1994], Lai et al. [2018].

Second, we used an adaptive gradient (AG) matching term that explicitly aligns spatial derivatives of the prediction and target:

$$\mathcal{L}_{AG} = \frac{1}{N} \sum_{i=1}^N \|\nabla \hat{y}_i - \nabla y_i\|_1, \quad (20)$$

which penalizes discrepancies in local edge/texture structure and further discourages blurring Mathieu et al. [2016], Xie et al. [2017].

Finally, we evaluated SPADE-style decoder conditioning with brain-region mask normalization to introduce spatially adaptive modulation of decoder activations, enabling region-dependent feature scaling guided by anatomical context Park et al. [2019]. Additionally, a 3D ResNet-18 classifier was trained for BRAAK grouping and used as a frozen feature extractor for optional feature-based supervision He et al. [2016], but this approach did not meaningfully improve results.

The evaluation used a 83 subject validation cohort. Metrics were reported as mean±standard deviation over subjects. We measured voxel wise reconstruction on raw PET and SUVR normalized PET, preservation of high uptake regions using thresholded masks, regional SUVR agreement using Bland Altman analysis on regional means, downstream BRAAK staging performance, and PID based Shapley attribution of redundant, unique, and complementary MRI contributions.

4.1 Raw Tau-PET and SUVR Voxelwise Reconstruction

Voxelwise reconstruction performance was measured on raw PET volumes and on SUVR-normalized PET volumes. Metrics included MAE, MSE, PSNR, SSIM, and MS-SSIM, where MAE and MSE quantified absolute and squared intensity error, PSNR summarized distortion in dB, and SSIM and MS-SSIM reflected structural similarity

Horé and Ziou [2010]. Regional SUVR agreement was summarized with relative SUVR error (%), defined as the mean absolute percent difference between predicted and reference regional SUVR means across ROIs and subjects.

Table 2 summarizes raw and SUVR reconstruction performance. DQ2H-MSE-Inf achieves the best raw PET fidelity, with MAE 0.1043 and PSNR 18.53. UNet+SPADE-VCC yields the highest raw SSIM at 0.863, consistent with stronger structural similarity. On SUVR PET, UNet+SPADE-MSE achieves the lowest SUVR MAE at 0.2914 and the lowest relative SUVR error at 12.8%, while DQ2H-MSE-Inf remains comparable with SUVR MAE 0.2918 and relative error 13.1%. As expected, SUVR normalization reduces dynamic range variation and compresses voxel-wise separation across the top models.

4.2 High Tau contrast preservation

High-uptake voxels carried clinical relevance because tau binding often appeared as spatially sparse, high-intensity signal Maass et al. [2017], Jack et al. [2018]. Preservation of these regions was assessed using thresholded high-uptake masks Coomans et al. [2025]. Metrics included lesion Dice between reference and predicted masks Dice [1945], Taha and Hanbury [2015], and voxel-wise sensitivity and specificity for high-uptake detection.

Table 3: High-contrast preservation on thresholded high-uptake masks (mean±std over subjects). Best values per column were bolded.

Model	Dice ↑	Sens. ↑	Spec. ↑
VAE-MSE	0.124±0.110	0.091±0.096	0.940±0.067
VQVAE-MSE	0.159±0.147	0.120±0.127	0.925±0.074
UNet-MSE	0.161±0.129	0.118±0.118	0.947±0.055
UNet+SPADE-MSE	0.507±0.165	0.513±0.196	0.827±0.109
UNet+SPADE-AG	0.037±0.036	0.026±0.029	0.809±0.082
UNet+SPADE-VCC	0.570±0.166	0.636±0.194	0.771±0.137
UNet+SPADE-MSE-AG	0.561±0.168	0.632±0.201	0.758±0.141
UNet+SPADE-VCC-AG	0.542±0.170	0.574±0.206	0.796±0.124
DQ2-MSE	0.082±0.079	0.064±0.070	0.973±0.043
DQ3-MSE	0.212±0.156	0.156±0.165	0.913±0.076
DQ2H-MSE	0.503±0.167	0.519±0.203	0.806±0.121
DQ2H-MSE-R18	0.171±0.134	0.118±0.121	0.962±0.047
DQ2H-MSE-Inf-R18	0.378±0.160	0.320±0.169	0.904±0.078
DQ2H-MSE-Inf	0.539±0.182	0.605±0.212	0.754±0.150
DQ2H-VCC-Inf	0.391±0.160	0.353±0.171	0.882±0.091
DQ2H+SPADE-MSE-Inf	0.430±0.165	0.399±0.185	0.868±0.106
DQ2H+SPADE-VCC-Inf	0.430±0.164	0.406±0.189	0.862±0.108

Table 3 indicates that UNet+SPADE-VCC achieves the best Dice (0.570) and sensitivity (0.636), consistent with improved recovery of high-uptake regions. DQ2H-MSE-Inf follows closely, with Dice 0.539 and sensitivity 0.605, while also providing stronger downstream BRAAK performance (Section 4.4). SPADE conditioning and contrast-aware losses increase high-contrast recovery, but downstream utility depends on joint preservation of structure, intensity, and regional disease patterns.

4.3 Bland–Altman analysis (Model vs GT SUVR agreement)

Regional SUVR agreement was assessed using Bland–Altman analysis Bland and Altman [1986]. For each subject and ROI, mean SUVR $(\hat{s} + s)/2$ was compared against percent SUVR error $(\hat{s} - s)/s \times 100$. Bias was defined as mean percent error. The 95% limits of agreement were defined as bias $\pm 1.96\sigma$.

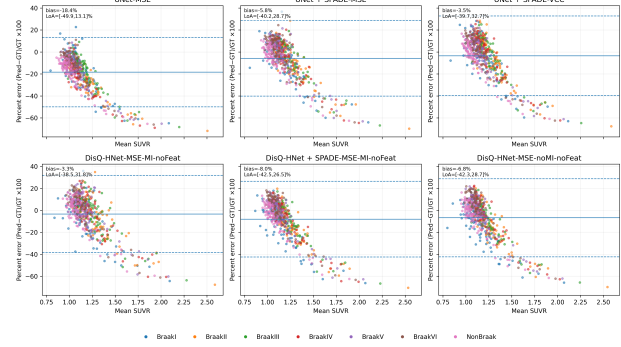


Figure 4: Bland–Altman plots of percent regional SUVR error for six models. Each point corresponded to one ROI from one subject. Horizontal lines indicated bias and 95% limits of agreement.

Table 4: Bland–Altman summary for percent regional SUVR error pooled over subjects and ROIs. Bias was the mean percent error. Limits of agreement were bias $\pm 1.96\sigma$.

Model	Bias (%)	95% LoA (%)
UNet-MSE	-18.4%	[-60.8, 23.9]%
UNet+SPADE-MSE	-8.2%	[-50.7, 34.3]%
UNet+SPADE-VCC	-3.5%	[-49.8, 42.7]%
DQ2H-MSE-Inf	-3.3%	[-43.1, 36.5]%
DQ2H+SPADE-MSE-Inf	-8.0%	[-50.1, 34.2]%
DQ2H-MSE	-9.2%	[-52.2, 33.8]%

Figure 4 and Table 4 indicate systematic SUVR underestimation in UNet-MSE (bias -18.4%). Conditioning and quantization reduce bias, with DQ2H-MSE-Inf at -3.3% and UNet+SPADE-VCC at -3.5% . Limits of agreement remain wide across models, consistent with strong subject and ROI dependence. Reduced bias remains important for staging because BRAAK assignment depends on thresholded regional SUVR.

4.4 BRAAK staging for clinical interpretation

BRAAK staging performance was evaluated by applying the SUVR-based staging pipeline to synthesized PET. Reported metrics included hard accuracy, soft accuracy with stage distance weighting (exact 1.0, off by 1 stage 0.6667, off by 2 stage 0.3333, off by 3 stage 0.0), and binary CN versus AD accuracy with AD defined as Braak \geq I/II.

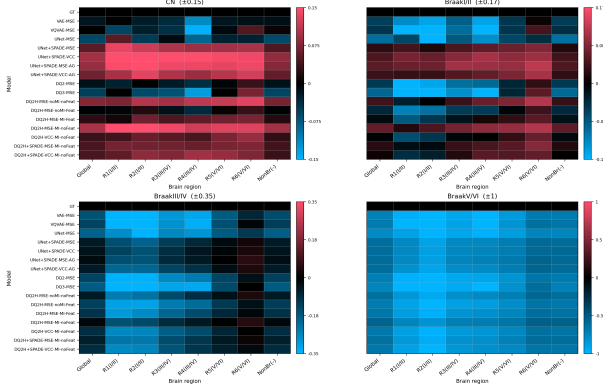


Figure 5: Stage-stratified regional SUVR bias patterns across synthesis models.

Table 5: Downstream BRAAK staging from synthesized PET (mean \pm std over subjects). Best values per column were bolded.

Model	Hard \uparrow	Soft \uparrow	CN/AD \uparrow
VAE-MSE	0.096 \pm 0.297	0.450 \pm 0.347	0.229 \pm 0.257
VQVAE-MSE	0.096 \pm 0.297	0.454 \pm 0.343	0.200 \pm 0.232
UNet-MSE	0.096 \pm 0.297	0.462 \pm 0.332	0.229 \pm 0.257
UNet+SPADE-MSE	0.434 \pm 0.497	0.755 \pm 0.246	0.800 \pm 0.244
UNet+SPADE-AG	0.096 \pm 0.297	0.450 \pm 0.347	0.229 \pm 0.257
UNet+SPADE-VCC	0.434 \pm 0.497	0.755 \pm 0.246	0.771 \pm 0.288
UNet+SPADE-MSE-AG	0.434 \pm 0.497	0.747 \pm 0.259	0.829\pm0.213
UNet+SPADE-VCC-AG	0.361 \pm 0.482	0.723 \pm 0.265	0.771 \pm 0.288
DQ2-MSE	0.084 \pm 0.278	0.454 \pm 0.343	0.200 \pm 0.232
DQ3-MSE	0.084 \pm 0.278	0.446 \pm 0.348	0.200 \pm 0.232
DQ2H-MSE	0.386 \pm 0.490	0.715 \pm 0.290	0.743 \pm 0.280
DQ2H-MSE-R18	0.120 \pm 0.325	0.510 \pm 0.332	0.286 \pm 0.323
DQ2H-MSE-Inf-R18	0.289 \pm 0.457	0.639 \pm 0.295	0.571 \pm 0.323
DQ2H-MSE-Inf	0.482\pm0.503	0.779\pm0.251	0.800 \pm 0.244
DQ2H-VCC-Inf	0.289 \pm 0.457	0.639 \pm 0.295	0.571 \pm 0.323
DQ2H+SPADE-MSE-Inf	0.458 \pm 0.501	0.723 \pm 0.265	0.829\pm0.213
DQ2H+SPADE-VCC-Inf	0.325 \pm 0.471	0.647 \pm 0.287	0.629 \pm 0.302

Stage-stratified regional SUVR percent errors and ROI-wise Pearson correlations were also reported to connect fidelity to regional disease patterns.

Table 5 shows the strongest overall downstream performance for DQ2H-MSE-Inf, with hard accuracy 0.482 and soft accuracy 0.779, while maintaining competitive reconstruction metrics. Several top models reach CN versus AD accuracy near 0.80, indicating preservation of coarse disease signal. DQ2H-MSE-Inf provides the most consistent improvement across fidelity and staging.

Table 6 shows increasing regional SUVR error with disease stage across all models, with the largest errors in Braak V/VI. DQ2H-MSE-Inf shows positive correlations in early BRAAK ROIs (I to III), while several UNet baselines show near-zero or negative correlations, consistent with weaker preservation of stage-relevant regional ordering.

Table 6: Regional SUVR agreement for representative models. Top block: absolute percent SUVR error on regional means by subject stage. Bottom block: ROI-wise Pearson correlation r across all subjects.

Abs. percent SUVR error (%)							
Model	ALL	CN	Braak I/II	Braak III/IV	Braak V/VI		
UNet-MSE	31.2 \pm 22.9	34.5 \pm 23.4	28.1 \pm 18.5	34.8 \pm 25.1	41.6 \pm 26.2		
UNet+SPADE-MSE	12.8 \pm 13.3	15.1 \pm 14.4	12.0 \pm 10.0	11.4 \pm 12.0	17.7 \pm 15.0		
UNet+SPADE-VCC	13.4 \pm 13.7	15.9 \pm 14.9	12.6 \pm 10.6	12.2 \pm 13.0	18.2 \pm 15.2		
DQ2H-MSE-Inf	13.9 \pm 14.8	17.2 \pm 16.1	6.4 \pm 5.8	8.8 \pm 8.4	28.8 \pm 18.7		
DQ2H+SPADE-MSE-Inf	18.5 \pm 17.9	23.0 \pm 19.8	11.2 \pm 9.7	12.8 \pm 11.2	37.2 \pm 21.6		
DQ2H-MSE	15.8 \pm 15.9	19.2 \pm 16.9	9.1 \pm 8.0	10.6 \pm 9.9	31.5 \pm 20.2		
Pearson r (ALL subjects)							
Model	I	II	III	IV	V	VI	Non-Braak
UNet-MSE	-0.18	-0.26	-0.08	-0.03	-0.15	0.13	0.07
UNet+SPADE-MSE	-0.11	-0.04	-0.11	-0.05	-0.13	0.18	0.08
UNet+SPADE-VCC	-0.11	-0.04	-0.11	-0.05	-0.14	0.18	0.09
DQ2H-MSE-Inf	0.16	0.20	0.24	0.03	0.14	-0.01	0.05
DQ2H+SPADE-MSE-Inf	-0.07	0.03	0.14	0.04	0.09	0.01	0.07
DQ2H-MSE	-0.05	0.03	0.13	0.06	0.04	-0.02	0.04

4.5 Shapley analysis of PID components

Information contribution in the PID-based model was analyzed by decomposing the latent representation into structure, redundant, unique $_{T1}$, unique $_{T2}$, and complementary components. Shapley values were computed over coalitions using structure-only as the baseline, consistent with cooperative game-theoretic credit assignment where each player’s attribution is its average marginal contribution across all coalitions Shapley [1953], Lundberg and Lee [2017], Chen et al. [2023]. In multimodal settings, Shapley-style coalition analysis has also been used to quantify modality-specific contribution and cross-modal cooperation Hu et al. [2022].

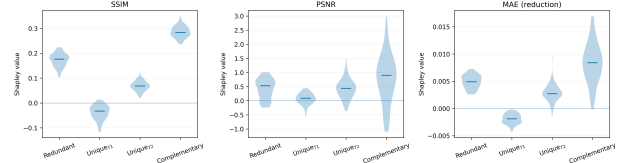


Figure 6: Per-subject PID-Shapley distributions for SSIM, PSNR, and MAE reduction $\Delta(-MAE)$.

Table 7: PID-Shapley attribution for the PID model (mean \pm std over subjects). Shapley values quantified marginal contribution relative to structure-only. MAE was reported as $\Delta(-MAE)$.

Component	$\Delta(-MAE)$	$\Delta PSNR$	$\Delta SSIM$
Redundant	0.0022 \pm 0.0018	0.22 \pm 0.46	0.095 \pm 0.018
Unique $_{T1}$	-0.0003 \pm 0.0013	-0.02 \pm 0.36	-0.018 \pm 0.014
Unique $_{T2}$	0.0023 \pm 0.0015	0.18 \pm 0.39	0.096 \pm 0.016
Complementary	0.0084 \pm 0.0036	0.77 \pm 0.85	0.286 \pm 0.023

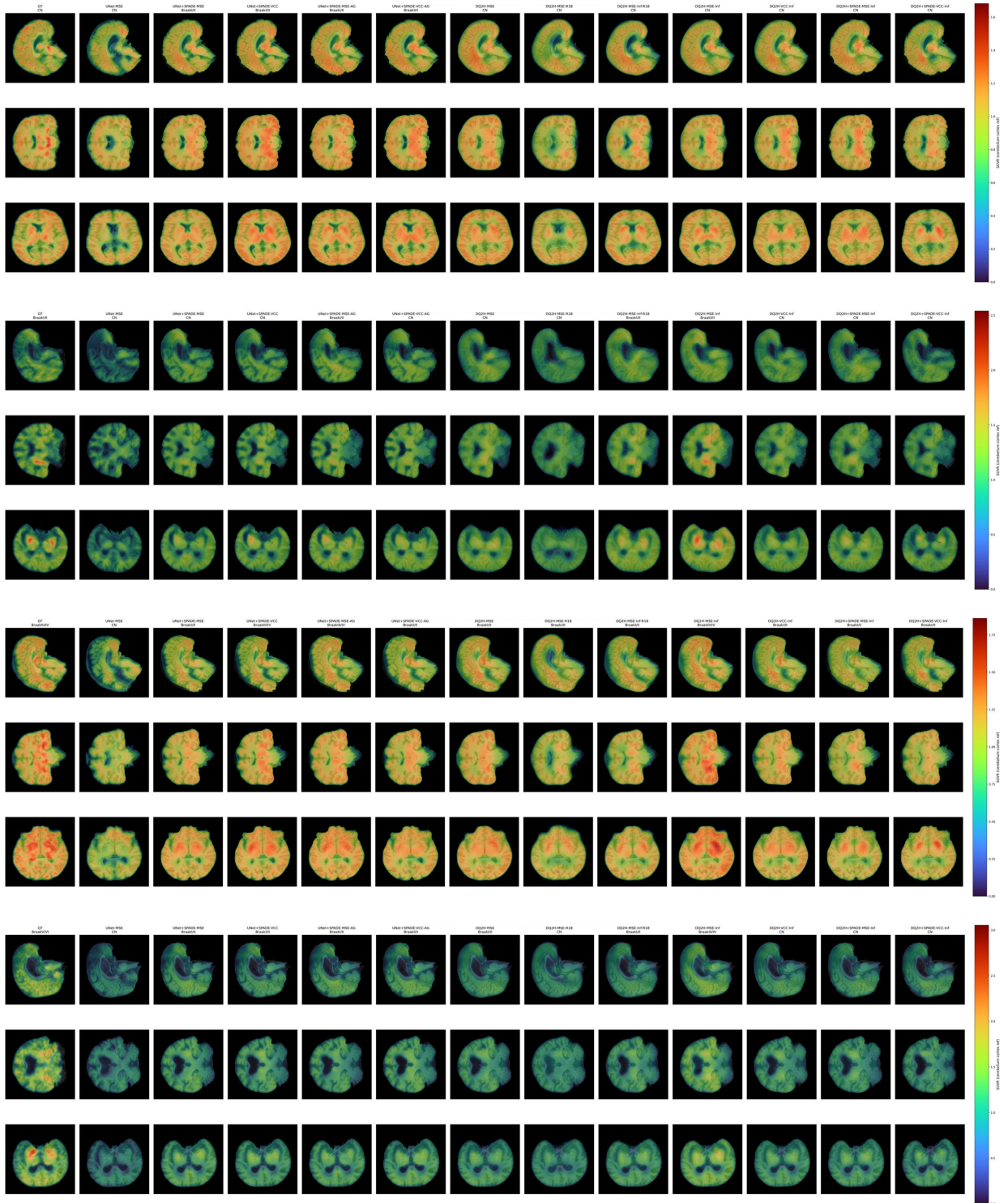


Figure 7: Qualitative SUVR reconstructions across BRAAK stages.

Table 8 indicates the largest single-component gain after adding complementary information to the structure stream, with the strongest improvement in perceptual similarity. Unique_{T1} contributes limited PET-specific benefit. Table 7 and Figure 6 show the largest marginal gains from complementary component, followed by redundant and

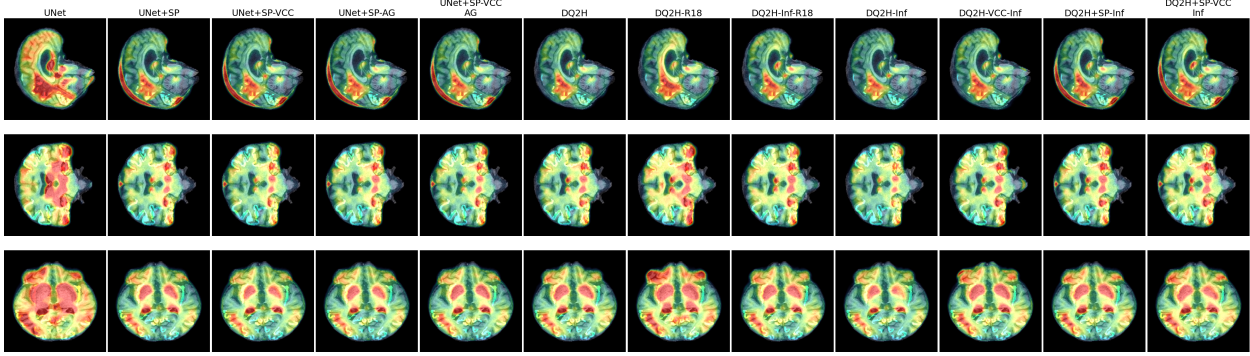


Figure 8: Cohort-level error hot-spot visualization: mean voxelwise SUVR MSE overlaid on the validation subject-0 T1 template ($N=83$).

Table 8: PID coalition reconstructions (mean \pm std). Each row combined the structure stream with the listed PID component(s).

Coalition	MSE \downarrow	MAE \downarrow	PSNR \uparrow	SSIM \uparrow	MS-SSIM \uparrow
Structure	0.0059 \pm 0.0037	0.0424 \pm 0.0109	22.82 \pm 2.06	0.322 \pm 0.020	0.771 \pm 0.033
Redundant	0.0050 \pm 0.0034	0.0332 \pm 0.0111	23.65 \pm 2.32	0.647 \pm 0.032	0.809 \pm 0.033
Unique $_{T1}$	0.0057 \pm 0.0036	0.0470 \pm 0.0113	23.04 \pm 2.13	0.232 \pm 0.019	0.788 \pm 0.035
Unique $_{T2}$	0.0051 \pm 0.0034	0.0367 \pm 0.0113	23.65 \pm 2.31	0.450 \pm 0.028	0.810 \pm 0.034
Complimentary	0.0049 \pm 0.0032	0.0306 \pm 0.0107	23.77 \pm 2.34	0.763 \pm 0.039	0.811 \pm 0.033
Full	0.0043 \pm 0.0031	0.0281 \pm 0.0109	24.49 \pm 2.54	0.810 \pm 0.028	0.843 \pm 0.035

unique $_{T2}$. Unique $_{T1}$ shows small negative contributions for SSIM and MAE reduction, consistent with a primary role in anatomical scaffolding. Shapley contributions remain stable across subject stages, consistent with a persistent role of cross-modal interaction across disease severity.

4.6 SUVR and model error hot-spot visualizations

We complement quantitative metrics with qualitative comparisons of synthesized SUVR appearance across disease stage. Figure 7 presents representative sagittal/coronal/axial slices for cognitively normal (CN) and increasing Braak groups for ground truth and top models tested. To summarize systematic failure modes at the cohort level, Fig. 8 overlays the mean voxelwise SUVR *MSE* (averaged over the $N=83$ validation subjects) on patient 0 T1 template using T1 reregistration transform, providing an interpretable *hot-spot map* of where errors concentrate across the brain. Together, these visualizations complement aggregate scores by localizing consistent error patterns and highlighting regions where residual bias persists.

5 Discussion

High image fidelity did not imply clinical utility. Several models achieve strong SSIM and PSNR but differ substantially in downstream BRAAK performance. DQ2H-MSE-Inf combines strong raw PET fidelity with the best hard and soft BRAAK accuracy (Table 2, Table 5). Models with

degraded intensity structure show degraded reconstruction and staging.

SUVR calibration remains a major error source. Bland-Altman analysis shows systematic underestimation in UNet-MSE (bias -18.4%), with reduced bias under SPADE conditioning and PID-based quantization (Table 4, Figure 4). Limits of agreement remain wide, consistent with subject and ROI dependence. Stage-stratified results show increased SUVR error in Braak V/VI (Table 6), consistent with broader cortical involvement and higher uptake heterogeneity.

PID-Shapley analysis supports a mechanistic explanation for downstream gains. Complementary information provides the largest marginal contribution across metrics (Table 7, Figure 6). This pattern supports a role for cross-modal interaction in explaining uptake patterns beyond either modality alone. Unique $_{T1}$ provides limited or negative marginal value for PET-specific similarity, consistent with a primary contribution to anatomical scaffolding.

Evaluation requires multiple axes, including raw and SUVR fidelity, high-contrast preservation, SUVR agreement, and downstream staging. Within this protocol, DisQ-HNet provides a favorable balance of voxel fidelity, reduced SUVR bias, improved high-uptake recovery, and strong BRAAK performance, while supporting interpretable component-wise attribution.

6 Conclusion

MRI to tau-PET synthesis models were evaluated using raw and SUVR reconstruction metrics, high-uptake preservation, regional SUVR agreement, and downstream BRAAK staging. DisQ-HNet provides the strongest overall balance of reconstruction fidelity and clinical interpretability, with reduced SUVR bias and the best BRAAK hard and soft accuracy on the validation cohort. PID-based Shapley attribution identifies cross-modal complementary information as the dominant contributor to PET-specific fidelity. Late-

stage SUVR calibration and subject-dependent variability remain the primary limitations.

Acknowledgments

Juampablo Heras Rivera is supported by the U.S. Department of Energy, Office of Science, Office of Advanced Scientific Computing Research, DOE Computational Science Graduate Fellowship (Award No. DE-SC0024386). We thank Hershdeep Singh Chopra (Northwestern University) for PID insights and Ilka M. Lorenzo (Northwestern University) for biological expertise on brain aging and AD.

References

- Alzheimer’s Association. 2024 alzheimer’s disease facts and figures. *Alzheimer’s & Dementia*, 20(5):3708–3821, 2024. doi: 10.1002/alz.13809.
- G. Livingston, J. Huntley, A. Sommerlad, et al. Dementia prevention, intervention, and care: 2020 report of the lancet commission. *The Lancet*, 396(10248):413–446, 2020. doi: 10.1016/S0140-6736(20)30367-6.
- C. R. Jack, D. A. Bennett, K. Blennow, et al. NIA-AA research framework: Toward a biological definition of alzheimer’s disease. *Alzheimer’s & Dementia*, 14(4): 535–562, 2018. doi: 10.1016/j.jalz.2018.02.018.
- H. Braak and E. Braak. Neuropathological staging of alzheimer-related changes. *Acta Neuropathologica*, 82(4):239–259, 1991. doi: 10.1007/BF00308809.
- H. Braak and E. Braak. Staging of alzheimer’s disease-related neurofibrillary changes. *Neurobiology of Aging*, 16(3):271–278, 1995. doi: 10.1016/0197-4580(95)00021-6.
- S. C. Burnham, M. D. Devous, et al. A review of the flortaucipir literature for positron emission tomography imaging of tau neurofibrillary tangles. *Brain Communications*, 6(1):fcad305, 2024. doi: 10.1093/braincomms/fcad305.
- S.-D. Chen et al. Staging tau pathology with tau pet in alzheimer’s disease: A longitudinal study. *Translational Psychiatry*, 2021. doi: 10.1038/s41398-021-01602-5.
- Ruben Smith, Michael Schöll, Michael Honer, and K. Peter R. Nilsson. Tau positron emission tomography imaging using flortaucipir (av-1451): methods and clinical applications. *Journal of Internal Medicine*, 285(6):647–667, 2019. doi: 10.1111/joim.12852.
- Antoine Leuzy, Tharick A. Pascoal, Olof Strandberg, et al. Clinical applications of tau pet in alzheimer’s disease: current state and future directions. *Nature Reviews Neurology*, 2025. Advance online publication.
- J. Lee, B. J. Burkett, H.-K. Min, et al. Synthesizing images of tau pathology from cross-modal neuroimaging using deep learning. *Brain*, 147(3):980–995, 2024. doi: 10.1093/brain/awad346.
- G. B. Frisoni, N. C. Fox, C. R. Jack, P. Scheltens, and P. M. Thompson. The clinical use of structural mri in alzheimer disease. *Nature Reviews Neurology*, 6(2): 67–77, 2010. doi: 10.1038/nrneurol.2009.215.
- S. Dayarathna et al. Deep learning based synthesis of mri, ct and pet: Review and analysis. *Medical Image Analysis*, 92:103046, 2024. doi: 10.1016/j.media.2023.103046.
- Guang Yang, Qinghao Ye, and Jun Xia. Unbox the black-box for the medical explainable ai via multi-modal and multi-centre data fusion: A mini-review, two showcases and beyond. *Information Fusion*, 77:29–52, 2022. doi: 10.1016/j.inffus.2021.07.016.
- Dost Muhammad and Malika Bendeche. Unveiling the black box: A systematic review of explainable artificial intelligence in medical image analysis. *Computational and Structural Biotechnology Journal*, 24: 542–560, 2024. doi: 10.1016/j.csbj.2024.08.005.
- O. Ronneberger, P. Fischer, and T. Brox. U-net: Convolutional networks for biomedical image segmentation. In *MICCAI*, 2015.
- Phillip Isola, Jun-Yan Zhu, Tinghui Zhou, and Alexei A. Efros. Image-to-image translation with conditional adversarial networks. In *CVPR*, 2017.
- Xi Chen, Diederik P. Kingma, Tim Salimans, Yan Duan, Prafulla Dhariwal, John Schulman, Ilya Sutskever, and Pieter Abbeel. Variational lossy autoencoder. In *International Conference on Learning Representations (ICLR)*, 2017.
- Naftali Tishby and Noga Zaslavsky. Deep learning and the information bottleneck principle. In *IEEE Information Theory Workshop*, 2015.
- A. van den Oord, O. Vinyals, and K. Kavukcuoglu. Neural discrete representation learning. In *NeurIPS*, 2017a.
- Paul L. Williams and Randall D. Beer. Nonnegative decomposition of multivariate information. *arXiv preprint arXiv:1004.2515*, 2010. URL <https://arxiv.org/abs/1004.2515>.
- A. Kolchinsky. A novel approach to the partial information decomposition. *Entropy*, 24:403, 2022. doi: 10.3390/e24030403.
- Michael Wibral, Viola Priesemann, Jim W. Kay, Joseph T. Lizier, and William A. Phillips. Partial information decomposition as a unified approach to the specification of neural goal functions. *Brain and Cognition*, 112: 25–38, 2017. doi: 10.1016/j.bandc.2015.09.004.
- Aaron van den Oord, Oriol Vinyals, and Koray Kavukcuoglu. Neural discrete representation learning, 2018. URL <https://arxiv.org/abs/1711.00937>.
- Kyle Schick-Poland, Abdullah Makkeh, Aaron J. Gutknecht, Patricia Wollstadt, Anja Sturm, and Michael Wibral. A partial information decomposition for discrete and continuous variables, 2021. URL <https://arxiv.org/abs/2106.12393>.

- Seiya Tokui and Issei Sato. Disentanglement analysis with partial information decomposition, 2022. URL <https://arxiv.org/abs/2108.13753>.
- Aaron van den Oord, Oriol Vinyals, and Koray Kavukcuoglu. Neural discrete representation learning. In *NeurIPS*, 2017b.
- Ali Razavi, Aaron van den Oord, and Oriol Vinyals. Generating diverse high-fidelity images with vq-vae-2. In *NeurIPS*, 2019.
- Eric Jang, Shixiang Gu, and Ben Poole. Categorical reparameterization with gumbel-softmax. In *ICLR*, 2017.
- Chris J. Maddison, Andriy Mnih, and Yee Whye Teh. The concrete distribution: A continuous relaxation of discrete random variables. In *ICLR*, 2017.
- Thomas M. Cover and Joy A. Thomas. *Elements of Information Theory*. Wiley, 2006.
- Colin Studholme, Derek L. G. Hill, and David J. Hawkes. An overlap invariant entropy measure of 3d medical image alignment. *Pattern Recognition*, 32(1):71–86, 1999.
- Irina Higgins et al. beta-vae: Learning basic visual concepts with a constrained variational framework. In *ICLR*, 2017.
- Christopher P. Burgess et al. Understanding disentangling in beta-vae. *arXiv preprint arXiv:1804.03599*, 2018.
- Irwin Sobel and Gary Feldman. A 3x3 isotropic gradient operator for image processing. Technical report, Stanford Artificial Intelligence Project, 1968.
- Peter J. Burt and Edward H. Adelson. The laplacian pyramid as a compact image code. *IEEE Transactions on Communications*, 31(4):532–540, 1983.
- Mingxing Tan and Quoc V. Le. Efficientnet: Rethinking model scaling for convolutional neural networks. In *International Conference on Machine Learning*, volume 97 of *Proceedings of Machine Learning Research*, pages 6105–6114, 2019.
- Maithra Raghu, Chiyuan Zhang, Jon Kleinberg, and Samy Bengio. Transfusion: Understanding transfer learning for medical imaging. In *Advances in Neural Information Processing Systems (NeurIPS)*, volume 32, 2019.
- Christian Szegedy, Wei Liu, Yangqing Jia, et al. Going deeper with convolutions. In *CVPR*, 2015.
- Diganta Misra. Mish: A self regularized non-monotonic neural activation function. *BMVC*, 2019.
- Kaiming He, Xiangyu Zhang, Shaoqing Ren, and Jian Sun. Deep residual learning for image recognition. In *CVPR*, 2016.
- Dmitry Ulyanov, Andrea Vedaldi, and Victor Lempitsky. Instance normalization: The missing ingredient for fast stylization. *arXiv preprint arXiv:1607.08022*, 2016.
- Taesung Park, Ming-Yu Liu, Ting-Chun Wang, and Jun-Yan Zhu. Semantic image synthesis with spatially-adaptive normalization. In *CVPR*, 2019.
- Michael W. Weiner, Dallas P. Veitch, Paul S. Aisen, Laurel A. Beckett, Nigel J. Cairns, Robert C. Green, Danielle Harvey, Clifford R. Jr Jack, William Jagust, John C. Morris, Ronald C. Petersen, Josue Salazar, Andrew J. Saykin, Leslie M. Shaw, Arthur W. Toga, John Q. Trojanowski, and Alzheimer’s Disease Neuroimaging Initiative. The alzheimer’s disease neuroimaging initiative 3: Continued innovation for clinical trial improvement. *Alzheimer’s & Dementia*, 13(5):561–571, May 2017. doi: 10.1016/j.jalz.2016.10.006. URL <http://dx.doi.org/10.1016/j.jalz.2016.10.006>.
- Pamela J. LaMontagne, Tammie L.S. Benzinger, John C. Morris, Samuel Keefe, Robert Hornbeck, Chengjie Xiong, Emily Grant, Jason Hassenstab, Krista Moulder, Andrei G. Vlassenko, Marcus E. Raichle, Carlos Cruchaga, and Daniel Marcus. Oasis-3: Longitudinal neuroimaging, clinical, and cognitive dataset for normal aging and alzheimer disease. *bioRxiv*, 2019. doi: 10.1101/2019.12.13.19014902. URL <https://www.medrxiv.org/content/10.1101/2019.12.13.19014902v1>.
- Yann LeCun, Léon Bottou, Genevieve Orr, and Klaus-Robert Müller. Efficient backprop. *Neural Networks: Tricks of the Trade*, pages 9–50, 1998.
- Christian Ledig et al. Photo-realistic single image super-resolution using a generative adversarial network. In *CVPR*, 2017.
- Pierre Charbonnier, Laure Blanc-Féraud, Gilles Aubert, and Michel Barlaud. Two deterministic half-quadratic regularization algorithms for computed imaging. *ICIP*, 1994.
- Wei-Sheng Lai et al. Learning a deep convolutional network for image super-resolution. In *ECCV*, 2018.
- Michael Mathieu, Camille Couprie, and Yann LeCun. Deep multi-scale video prediction beyond mean square error. In *ICLR*, 2016.
- Lingxi Xie et al. All you need is beyond a good init: Exploring better solution for training extremely deep convolutional neural networks with orthonormality and modulation. In *CVPR*, 2017.
- Alain Horé and Djemel Ziou. Image quality metrics: Psnr vs. ssim. In *2010 20th International Conference on Pattern Recognition*, pages 2366–2369, 2010. doi: 10.1109/ICPR.2010.579.
- Anne Maass et al. Comparison of multiple tau-pet measures as biomarkers in alzheimer’s disease. *NeuroImage*, 157:448–463, 2017. doi: 10.1016/j.neuroimage.2017.05.058.
- Erik M. Coomans et al. Quantitation of pet spatial extent as a potential adjunct to standard measures: Tau-spex. *Journal of Nuclear Medicine*, 2025.
- Lee R. Dice. Measures of the amount of ecologic association between species. *Ecology*, 26(3):297–302, 1945. doi: 10.2307/1932409.

- Ahmed A. Taha and Allan Hanbury. Metrics for evaluating 3d medical image segmentation: analysis, selection, and tool. *BMC Medical Imaging*, 15:29, 2015. doi: 10.1186/s12880-015-0068-x.
- J. Martin Bland and Douglas G. Altman. Statistical methods for assessing agreement between two methods of clinical measurement. *The Lancet*, 327(8476):307–310, 1986. doi: 10.1016/S0140-6736(86)90837-8.
- Lloyd S. Shapley. A value for n-person games. In Harold W. Kuhn and Albert W. Tucker, editors, *Contributions to the Theory of Games II*, pages 307–317. Princeton University Press, 1953. doi: 10.1515/9781400881970-018.
- Scott M. Lundberg and Su-In Lee. A unified approach to interpreting model predictions. In *Advances in Neural Information Processing Systems (NeurIPS)*, 2017.
- Hugh Chen, Ian C. Covert, Scott M. Lundberg, and Su-In Lee. Algorithms to estimate Shapley value feature attributions. *Nature Machine Intelligence*, 5(6):590–601, 2023. doi: 10.1038/s42256-023-00657-x.
- Peiyang Hu et al. SHAPE: An unified approach to evaluate the contribution of individual modalities and the cooperation of multiple modalities. In *Proceedings of the International Joint Conference on Artificial Intelligence (IJCAI)*, 2022.